Published in final edited form as:
J Struct Biol. 2015 January ; 189(1): 44–52. doi:10.1016/j.jsb.2014.10.013.

Quantitative analysis of mouse pancreatic islet architecture by serial block-face SEM

C.R. Pfeifer[#1], **A. Shomorony**[#1], **M.A. Aronova**[1], **G. Zhang**[1], **T. Cai**[2], **H. Xu**[2], **A.L. Notkins**[2], and **R.D. Leapman**[1]

[1]National Institute of Biomedical Imaging and Bioengineering, National Institutes of Health, Bethesda, MD 20854, USA

[2]National Institute of Dental and Craniofacial Research, National Institutes of Health, Bethesda, MD 20854, USA

[#] These authors contributed equally to this work.

Abstract

We have applied serial block-face scanning electron microscopy (SBF-SEM) to measure parameters that describe the architecture of pancreatic islets of Langerhans, microscopic endocrine organs that secrete insulin and glucagon for control of blood glucose. By analyzing entire mouse islets, we show that it is possible to determine (1) the distributions of alpha and beta cells, (2) the organization of blood vessels and pericapillary spaces, and (3) the ultrastructure of the individual secretory cells. Our results show that the average volume of a beta cell is nearly twice that of an alpha cell, and the total mitochondrial volume is about four times larger. In contrast, nuclear volumes in the two cell types are found to be approximately equal. Although the cores of alpha and beta secretory granules have similar diameters, the beta granules have prominent halos resulting in overall diameters that are twice those of alpha granules. Visualization of the blood vessels revealed that every secretory cell in the islet is in contact with the pericapillary space, with an average contact area of 9 ± 5% of the cell surface area. Our data show that consistent results can be obtained by analyzing small numbers of islets. Due to the complicated architecture of pancreatic islets, such precision cannot easily be achieved by using TEM of thin sections.

Keywords

serial block face SEM; pancreatic islets of Langerhans; insulin secreting granules; glucagon secreting granules; 3D reconstruction

Corresponding authors: Richard D. Leapman, Ph.D., NIBIB, NIH tel: 301-496-2599; leapmanr@mail.nih.gov Abner L. Notkins, M.D., NIDCR, NIH tel: 301-496-4535; anotkins@mail.nih.gov.

1. Introduction

Islets of Langerhans are micro-organs comprising clusters of cells responsible for endocrine function in the pancreas. In a typical human pancreas, approximately one million islets predominate in the organ's tail region, where they are completely surrounded by acinar exocrine tissue (Stendahl et al., 2009). Despite only contributing 1-2% to the total pancreatic mass, islets are of critical importance in the body, synthesizing and secreting hormones that are crucial for glucose homeostasis and nutrient metabolism. Five types of hormone-secreting cells have been identified in the islets of Langerhans: glucagon-secreting alpha cells, insulin-secreting beta cells, pancreatic polypeptide-secreting F (or gamma) cells, somatostatin-secreting delta cells, and ghrelin-secreting epsilon cells (Cabrera et al., 2006; Prado et al., 2004).

Levels of circulating nutrients, such as plasma glucose, regulate the release of islet hormones into the hepatic portal vein. This controlled release is highly dependent on the spatial arrangement of islets and their constituent elements. Not only do islets communicate via paracrine (Gromada et al., 2007) and autocrine (Khan et al., 2001) interactions, but individual islet cells are believed to provide feedback to one another through, for example, electrical coupling between beta cells (Pérez-Armendariz et al., 1991) in order for the islet to achieve hormonal balance. One of the islet's key features, therefore, is the highly organized spatial pattern in which the islet's cells and its perfusing blood vessels are arranged. A proper understanding of the islet's cytoarchitecture through a detailed visualization of its entire ultrastructure can provide important new anatomical insight to improve our understanding of islet physiology.

Recently developed 3-D imaging techniques, based on electron microscopy of large tissue volumes, are well suited to this endeavor. In particular, two widely adopted approaches, for which blocks of tissue are prepared by heavy-atom staining and plastic embedding, are: (1) focused ion beam (FIB) milling of the block face in the scanning electron microscope (SEM) (Bennett et al., 2009; Drobne, 2013; Hekking et al., 2009; Schneider et al., 2010), and (2) serial block-face (SBF) ultramicrotomy of the block face in the SEM (Briggman et al., 2011; Denk and Horstmann, 2004; Helmstaedter et al., 2013). Both the FIB-SEM and SBF-SEM techniques allow imaging of large sample volumes at the nanometer scale with a pixel size of ~5 nm in the block face's *x*-*y* plane. FIB-SEM has the highest spatial resolution in the *z*-direction perpendicular to the block face because the focused ion beam can remove arbitrarily thin surface layers, but FIB milling is a relatively slow process, which typically limits the total volume that can be conveniently analyzed. Although SBF-SEM has a minimum pixel size of 25 nm in the *z*-direction, which is limited by the minimum slice thickness that the ultramicrotome can remove, the cutting process is fast so that SBF-SEM can analyze much larger volumes (~100 μm in every dimension) than are practicable with FIB-SEM.

Serial block-face SEM's impressive speed is attributable to the diamond-knife ultramicrotome built into the SEM chamber. In an automated process, the face of the sample block is imaged by backscattered electron detection, then raised by some set amount (typically 25-200 nm), and then shaved by the ultramicrotome to expose a new surface. By

repetition of this process, it is possible to quickly and easily acquire thousands of sequential block-face images, which show equivalent contrast to TEM images of conventionally stained sections (Denk and Horstmann, 2004). These SBF-SEM slices can then be rendered into three-dimensional ultrastructure using software such as ImageJ (Schneider et al., 2012) and Amira (FEI, Inc.). This technique has been applied to diverse biological samples, including protozoan parasites (Hughes et al., 2013), corneas (Young et al., 2014), retinae (Mustafi et al., 2013), cardiac tissue (Pinali et al., 2013), and pancreatic islets (Hoppa et al., 2012).

Using serial block-face SEM, we have visualized entire mouse islets of Langerhans and studied their morphology at four different levels of magnification: we imaged at (1) the global level, (2) at the level of microvasculature, (3) at the cellular and sub-cellular level, and (3) at the level of secretory granules. We have used progressively higher-resolution images—with pixel sizes as small as 5 nm in the plane of the block face and 25 nm in the perpendicular direction—to unveil details of an islet's ultrastructure, such as the branching of its capillaries through pericapillary spaces and morphological distinctions between alpha and beta cells, and to obtain quantitative data at different scales, such as blood vessel surface areas, organelle volumes and numbers of hormonal granules per cell. The analytical methods presented herein further demonstrate the potential for characterization of biological tissue through SBF-SEM. Moreover, these methods pave the way for a full structural investigation of the islet of Langerhans, and thus complement previous islet investigations conducted by electron tomography techniques (Noske et al., 2008).

2. Materials and Methods

2.1 Sample Preparation

Mouse pancreatic islets from 2-3-months-old male mice were isolated as described previously (Cai et al., 2011; Zhang et al., 2007). Briefly, mice were anaesthetized by intraperitoneal injection with ketamine (50 mg/kg). Collagenase solution (Sigma, Saint Louis, MO, USA) was injected into the bile duct to inflate the pancreas. After digestion, islets were manually selected and washed in Krebs–Ringer HEPES buffer, and cultured overnight in RPMI-1640 medium (Invitrogen, Carlsbad, CA, USA) before further experiments. All procedures were approved by the NIDCR Institutional Animal Care and Use Committee.

In preparing the islets for SBF-SEM, we followed a combinatorial heavy metal staining protocol developed by Mark Ellisman's laboratory at UCSD (Holcomb et al., 2013; West et al., 2010). The first step was aldehyde fixation: the islets were fixed for five minutes in a mixture of 2.5% glutaraldehyde and 2% formaldehyde in sodium cacodylate buffer with 2 mM calcium chloride. The islets were then fixed for another two to three hours on ice in the same solution, after which they were thrice rinsed with cold cacodylate buffer containing 2 mM calcium chloride (five minutes for each rinse).

Next came heavy metal staining: the islets were fixed in Reduced Osmium—a solution containing 3% potassium ferrocyanide in 0.3 M cacodylate buffer with 4 mM calcium chloride combined with an equal volume of 4% aqueous osmium tetroxide—for one hour on

ice. They were then placed in a 0.22 μm-Millipore-filtered 1 % thiocarbohydrazide (TCH) solution in ddH_2O for 20 minutes. The heavy metal staining phase concluded with fixation of the samples in 2% osmium tetroxide in ddH_2O for 30 minutes. Between each of the preceding steps, the samples were washed five times, three minutes each time, with ddH_2O. At last, the samples were placed in 1% aqueous uranyl acetate and left overnight at ~4°.

The following day, the samples were washed again with ddH_2O five times for three minutes each time, and were then processed with en bloc Walton's lead aspartate staining (Walton, 1979) by submerging the islets in a lead aspartate solution and placing them in an oven for 30 minutes. Then, after another five three-minute ddH_2O rinses, the samples were dehydrated and embedded in Epon-Araldite according to standard protocols.

The final sample preparation step was to mount the islets for SBF-SEM with the goal of minimizing specimen charging. Each resin-embedded islet was first mounted on an empty resin block to be trimmed under the microtome. Once the top of the stained islet was exposed, the islet was re-mounted, exposed-side down, on a special aluminum specimen pin (Gatan, Pleasanton, CA) using CircuitWorks Conductive Epoxy (CW2400), which served to electrically ground the tissue to the aluminum pin. Each re-mounted sample was then trimmed again to expose the other side of the islet, and was sputter-coated with a thin layer of gold.

2.2 Serial Block-Face Scanning Electron Microscopy

The trimmed resin-embedded, stained blocks were imaged using a Gatan 3View serial block-face imaging system installed on a Zeiss SIGMA-VP (variable pressure) SEM, operating at an accelerating voltage of 1.5 kV using a standard 30 μm condenser aperture. The SEM was operated in high vacuum. Data were collected in three modes: (1) low-magnification mode, used to visualize structure at the global scale, with a pixel size of 55.7 nm in the *x*-*y* plane and 50 nm along the z-axis; (2) intermediate-magnification mode, used to capture the microvasculature, with a pixel size of 24.3 nm in the *x*-*y* plane and 50 nm along the *z*-axis; and (3) high-magnification mode, suited to the cellular and sub-cellular scale and secretory granules, with a pixel size of 5.4 nm in the *x*-*y* plane and 25 nm along the *z*-axis.

2.3 Data Visualization and Measurements

The resulting datasets were assembled into volume files and aligned using DigitalMicrograph (Gatan), and then manually segmented into 3-D models in Amira (Fig. 1). Three-dimensional structures in image stacks containing hundred or thousands of 2D orthoslices, as illustrated in Fig. 1A, are traced individually in each plane (Fig. 1B), and are surface-rendered (Fig. 1C).

The volumes and surface areas of Amira 3-D models are measured by the software's “Material Statistics” and “SurfaceArea” modules, respectively. Using these modules, we obtained all of the three-dimensional size parameters reported in §3. All lengths, such as secretory granule diameters, were found using Amira's “3-D Length Measure” tool.

In taking volume measurements, we examined a total of 60 cell membranes, 40 nuclei, and 12 mitochondrial networks; in each case, half were from alpha cells and the other half were from beta cells. Our surface area measurements were gathered from 20 cell membranes, 20 nuclei, and 12 mitochondrial networks, once again evenly split between alpha and beta cells. All cell-type differentiation was performed by visual inspection, using such well-documented cues as secretory granule appearance (Björkman et al., 1963; Mikami and Mutoh, 1971; Orci, 1974) and cytoplasmic lucency (Lacy, 1957; Lazarus and Volk, 1964; Winborn, 1963).

The precise number of insulin granules in our model beta cell was determined by manual count. Because serial block-face SEM produces high-resolution visualizations of large tissue samples, this technique makes it possible to identify and count even such small organelles as secretory granules. Though possible, such an approach is too time- and labor-intensive to be practical, especially when it is necessary to analyze many cells. We are currently pursuing other SBFSEM-based approaches to determining the number of granules in a cell.

2.4 Assessment of cutting uniformity

To assess the capability of SBF-SEM for visualizing 3D ultrastructure, it is necessary to determine the quality of the cutting process by displaying *x*-*z* or *y*-*z* orthoslices through the 3D datasets acquired with a well defined electron dose. In this regard, the *x*-*y* image planes were first carefully aligned using the cross-correlation function in Digital Micrograph. It is known that plastic-embedding material undergoes mass loss and collapse under electron irradiation resulting in uneven cutting in the SBF-SEM. Such radiation damage causes the specimen to collapse in the z-direction so that the microtome knife sporadically misses cutting a layer off the surface of the block. In our high-resolution imaging of the block, we selected a probe current of 40 pA, a beam energy of 1.5 keV and a dwell time of 1.5 μs/pixel with a pixel size in the *x*-*y* plane of 5.4 nm, and a slice thickness along the *z*-axis of 25 nm. This gave an electron dose of approximately 12 electrons/nm^2. Typical *x*-*z* slices through a beta cell of a pancreatic islet dataset (Fig. 2A-C) are consistent with uniform cutting, as evident by the round-shaped dense cores of the insulin granules, and the continuity of the membranes around the granules.

3. Results and Discussion

Our morphological investigation consists of the multi-scale visualization, analysis and spatial rendering of SBF-SEM data of two mouse islets of Langerhans. We use four different scales of visualization, imaging at the global level (the entire islet), the level of microvasculature (environments comprising blood vessels and their surrounding pericapillary spaces), the cellular/sub-cellular level (individual cells and their organelles), and the level of secretory granules (hormone-secreting dense core vesicles).

3.1 Global scale: an overview of the islet's cytoarchitecture

The mean size of a wild-type mouse islet has been measured previously to be 116 ± 80 μm, where islet size is defined as the diameter of a circle that has the same area as the measured islet area (Kim et al., 2009). By this definition, both of our islets were found to be 178 ± 1

μm in size, according to their areas in the central slices shown in Fig. 3. The sizes of these islets are consistent with those described in the literature.

Islets 1 and 2 are typical not only in their size, but also in their cellular composition and arrangement. A typical mouse islet consists of 65-85% beta cells, which are concentrated in the islet's central core, along with 10-25% alpha and 5-10% delta/other cells, which are localized in the islet's periphery (Brissova et al., 2005; Carter et al., 2009; Kharouta et al., 2009; Steiner et al., 2010). These relative cell-type proportions were observed in the two islets examined in this study. Moreover, both islets exhibited the standard rodent architecture, with beta cells filling out the centers of the islets and alpha, delta, and other cells studding their perimeters (Fig. 3).

3.2 Microvasculature: quantitative analysis of the islet's blood vessels and their environs

Two independently branching blood vessels from islet 1 were fully rendered in three dimensions (Fig. 4), and physical parameters pertaining to the blood vessel environment were calculated for one of the vessels (Table 1, Fig. 5). Before presenting these measurements, it is important to state that quantitative analysis of blood vessel and pericapillary volumes could be significantly affected by the islet dissection and subsequent aldehyde fixation. In future, it would be preferable to prepare islets by high-pressure freezing and freeze-substitution. Nevertheless, results from chemically fixed preparations provide a useful preliminary view of the blood vessel organization in the pancreatic islet.

With this proviso, all blood vessels were found entirely surrounded by pericapillary spaces, empty spaces—accounting for 9.0 ± 0.3% of the islet's volume (Fig. 4)—into which hormones are secreted by endocrine cells before entering blood vessels through fenestrations in the endothelial cell walls (Camussi et al., 2008). Here, the volume fraction of the pericapillary space was determined from measurements of the cross sectional area of pericapillary spaces relative to the cross sectional area of the entire islet for different slices throughout the islet with the error expressed as a standard deviation. The space's role as a zone of mediation between blood and endocrine tissue cells fulfills the islet's crucial need for efficient perfusion. Rather than having much more numerous blood vessels touching every islet cell, the islet has a volume of pericapillary space four times as great as the volume enclosed by its blood vessels. Without space between the endocrine tissue and the endothelium, we estimate, based on the total pericapillary space and blood vessel surface areas (Table 1), that an islet would need to be at least twice as dense with blood vessels to perfuse all of its cells.

It was found, in a full three-dimensional analysis of islet 1, that every cell in the islet was in contact with either the outside of the islet or a pericapillary space in the islet. As shown in Table 1, the average contact area of a cell with the pericapillary space is 9 ± 5% of a typical beta cell's surface area. The calculation yielding this value, however, includes both cells in contact with just one blood vessel branch and cells in contact with two blood vessel branches, for which the average areas of contact as percentages of cell surface area are 8 ± 3% and 10 ± 6%, respectively.

Fig. 5 provides new—albeit preliminary—insights into the organization of islet capillaries and their surrounding endocrine cells, as well as the effect of branching on their spatial arrangement. In this three-dimensional rendering, we intend not to misrepresent the pericapillary space (blue) as a physical and textural compartment, but simply to demarcate the separation between the endothelium and the endocrine tissue. As expected, the total blood vessel volume remains constant between regions 1 and 3 as two thinner branches merge into a thicker branch. Branching is used to increase the blood vessel's surface area and to reach out to more cells, as can be seen by the highest blood-vessel surface area in region 1, and its magnified effect for pericapillary space surface area. Just as branching appears to be one solution to increase the blood vessel's accessibility to endocrine tissue, widening of the pericapillary space in unbranched regions seems to achieve a similar goal: the volume of pericapillary space is largest in region 3.

Three blood flow patterns have been predominantly reported for the islet: from perimeter non-beta cells towards core beta cells (Murakami et al., 1993; Ohtani, 1984), from core beta cells towards perimeter non-beta cells (Bonner-Weir, 1993; Stagner and Samols, 1986), and from one side of the islet to the other, regardless of cell type (Liu et al., 1993). The longer of our two fully-rendered blood vessels (Fig. 5A) has a total length of only ~62 μm between its entry into the islet and its exit out of the islet; given the islet's long and short axes of 233 ± 5 μm and 164 ± 5 μm (Fig. 4), respectively, this vessel cannot be said to travel through the islet's core. Due to the sample preparation method, which includes the dissection and dehydration of the islet and its vessels, the direction of this vessel's blood flow cannot be determined. The vessel, therefore, cannot be classified into one of the three widely suggested flow models. Unlike in most islet blood flow models, which describe a wider feeding arteriole that branches into capillaries in the islet (Nyman et al., 2008), our rendered vessel's diameter ranged from 5 μm to 10 μm, which is consistent with mouse islet capillary diameters (Christoffersson et al., 2010; Dai et al., 2013), throughout its entire length.

3.3 Cellular and sub-cellular scale: structural comparison of alpha and beta cells

Our comparison between alpha and beta cells complements formerly reported investigations on islet morphology and provides new insights based on higher-resolution imaging and quantitative measurements.

We found the endoplasmic reticulum (ER) of beta cells to be less prominent than the ER of alpha cells, in agreement with previous reports (Like and Chick, 1970; Munger et al., 1965). The decreased prominence of the ER in beta cells cannot just be attributed to the higher level of staining in the cytoplasm due to the presence of granular ER (Lacy, 1957; Munger et al., 1965) and microvesicles (Orci, 1982). We found the ER cisternae of the alpha cell to spread further than those of the beta cell, extending to 1.4 ± 0.6 μm in the alpha cell compared to 0.8 ± 0.5 μm in the beta cell, in any 2-D cross section. In contrast, cisternae of the Golgi apparatus appear more prominent in beta cells than in alpha cells, although we have not yet quantified these differences.

Mitochondria in alpha and beta cells have distinct morphologies with mitochondrial widths significantly narrower in alpha cells than in beta cells as evident from the two-dimensional slices presented in Figs. 6C and 6D. Analysis of 100 mitochondria in each cell type showed

that alpha cell mitochondria had a width of 253±83 nm, whereas beta cell mitochondria had a width of 329±92 nm (Fig. 7). In three-dimensional visualizations, shown in Fig. 8, both alpha and beta cell mitochondria are highly branched with the beta cell mitochondria occupying a greater percentage of the cellular volume (7.7%) than that occupied by the alpha-cell mitochondria (3.7%), as seen from Table 2.

Whereas beta and alpha cells were found to be similarly non-spherical, the cells' nuclei have distinctive shapes: beta cell nuclei tend to be more round and alpha cell nuclei, more pleiomorphic. This characteristic difference is apparent in SBF-SEM visualizations of both cell types (Fig. 8). By analyzing the volumes and surface areas of 10 beta and 10 alpha cell nuclei, it was found that the nucleus of beta cells had a sphericity of 0.78±0.02 compared with a sphericity of 0.59±0.09 for the nucleus of alpha cells, where the uncertainties are given as standard deviations. Here, sphericity Ψ is defined as the ratio of the surface area of a sphere (with volume equal to the measured volume *V*) to the measured surface area *S*:

$$\psi = \frac{(36\pi)^{\frac{1}{3}}(V)^{2/3}}{S}$$

Despite this difference in nuclear shape, alpha and beta cell nuclei tend to have very similar volumes: (1.3±0.12) × 10^2 μm^3 and (1.2±0.13) × 10^2 μm^3, respectively (Table 2). While recent studies have proposed a mechanism whereby nuclear size is determined by cytoplasmic volume (Neumann and Nurse, 2007), our data seem initially more consistent with the nucleoskeletal theory, which suggests that nuclear volume is determined largely by DNA content (Cavalier-Smith, 2005; Gregory, 2005). This theory, however, does not explain why cells from different tissues in a given organism can have varied nuclear sizes despite having the same amount of DNA (Altman and Katz, 1976). It is likely, therefore, that a combination of cytoplasmic factors (Webster et al., 2009) and a minimum size set by DNA content (Cavalier-Smith, 2005; Gregory, 2005) determine nuclear size in the alpha and beta cells. Given the difference in endoplasmic reticulum prominence in these cells (as explained above) and proposed mechanisms of reformation of nuclear envelope from ER reorganization (Anderson and Hetzer, 2007; Kiseleva et al., 2007), we suspect that membrane availability—higher in alpha cells than in beta cells— may be an important limiting factor in determining nuclear size. Not only do alpha-cell nuclei occupy a larger percentage of total cell volume, but they have larger surface areas than beta-cell nuclei (Table 2). The observed differences in nuclear size and shape between cell types, therefore, may be linked to the different levels of organization and availability of endoplasmic reticulum in these cells.

3.4 Secretory granules: the number, size, and haloed appearance of secretory granules in islet cells

The total number of insulin-secreting granules (ISGs) in our model beta cell, determined by manual count to be 11,700 ± 100, falls within the range of previously reported values, which spans from ~5,000 to 13,060 ISGs (Dean, 1973; Fava et al., 2012; Olofsson et al., 2002; Straub et al., 2004). This range is wide because the values were determined by TEM-based stereological methods, which lack the exactitude of SBF-SEM-based methods. Only full-cell

volume analysis, such as that enabled by SBF-SEM or FIB-SEM, quickly and easily reproduces every secretory granule in a cell, allowing those granules to be individually counted, either manually or via an automated counting algorithm.

The appearance of halos in islet secretory granules has been well documented by electron microscopy investigations of islets (Bencosme and Pease, 1958; Lacy and Davies, 1957; Like and Chick, 1970; Unger and Orci, 1976). Previous investigations have noted that glucagon-secreting granule (GSG) halos are visibly smaller than ISG ones, reporting that GSGs have membrane and dense core diameters of ~270 and ~200 nm, respectively (a ratio of 1.4), whereas ISGs have membrane and dense core diameters of ~360 and ~200 nm, respectively (a ratio of 1.8) (Barg et al., 2000; Fava et al., 2012; Huang et al., 2013; Olofsson et al., 2002). These published diameter measurements are in reasonabl e agreement with our own as evident in Fig. 9, Table 3, which reveal that that the core diameters of GSGs and ISGs are clustered around a similar mean value (230 nm and 240 nm, respectively). By contrast, GSGs have much thinner halos and much smaller membrane diameters than ISGs.

Several hypotheses have been proposed to explain the appearance of halos. Some assert that halos occur *in vivo*, and that granules naturally consist of an insoluble phase (i.e. a condensed core of glucagon or insulin) and a soluble phase (i.e. a halo of primarily precursor hormone) (Michael, 2006; Sobota et al., 2006; Westermark et al., 1996). Others claim instead that halos are artifacts of the sample preparation process in that they are created when chemical fixation causes granule membranes to either: (a) swell—and rupture—around cores that resist expansion on crystallization, or (b) shrink and tear away from their cores, producing space between the two. In support of the artifact hypothesis, Eugenio Fava and colleagues have reported that samples prepared by high-pressure freezing (HPF) show markedly fewer secretory granule halos than those prepared by traditional chemical fixation (Fava et al., 2012).

Although our SBF-SEM data do not provide decisive evidence for or against any of the above hypotheses, they do provide some additional insight. First, we did not observe routine fracturing of granule membranes, leading us to believe that either most membranes are intact or—less likely—their fractures are beyond the 5 nm resolution of our data. This finding casts doubt on the membrane swelling hypothesis, as it seems improbable for the average granule membrane to expand its surface area by such a large amount (170% for GSGs and 300% for ISGs) without rupturing. Second, in an as yet unpublished experiment in our lab, we looked at HPF islets using SBF-SEM, and we observed halos on most GSGs and ISGs (Supporting Fig. 1). We have not yet measured the sizes of these halos or rigorously quantified their frequency, but preliminary visual inspection suggests that HPF does not necessarily eliminate—or even lessen—the appearance of halos, as previously thought. Clearly, further experimentation is needed to ascertain why secretory granule halos show up in electron micrographs of pancreatic islets.

4. Conclusions

We have demonstrated that new quantitative parameters describing the multi-scale three-dimensional architecture of mouse pancreatic islets of Langerhans can be derived using

SBFSEM. By analyzing entire islets with this approach, it is possible to determine the total numbers and distributions of alpha and beta cells, the organization of blood vessels and pericapillary spaces that perfuse these microscopic endocrine organs, and the ultrastructure of the individual secretory cells. We found that the mean cellular volume of beta cells was nearly twice that of alpha cells, and the mitochondrial volume of beta cells about four times that of alpha cells, whereas nuclear volumes in the two cell types were approximately equal. Cores of the alpha and beta secretory granules have roughly equal diameters, but beta granules have twice the membrane diameter of alpha granules. Visualization of the blood vessels revealed that the plasma membrane of every secretory cell in the islet contributed to the surface of the pericapillary space, with an average contact area of 9 ± 5% of the cell surface area. Overall, the pericapillary space comprised 9% of the islet volume. Due to the considerable geometrical complexity of pancreatic islets, this type of quantitative information is very difficult to obtain from conventional TEM based on stereological measurements on thin sections. With our approach, it becomes feasible to quickly and accurately quantify islets' structural parameters, making it possible to study islets at different stages of development, compare normal and disease model islets, and ultimately examine human islets with unprecedented detail.

Supplementary Material

Refer to Web version on PubMed Central for supplementary material.

Acknowledgment

This work was supported by the Intramural Research Program of the National Institutes of Biomedical Imaging and Bioengineering, and the National Institute of Dental and Craniofacial Research, NIH.

References

Altman, PL.; Katz, DD. Cell Biology. Federation of American Societies for Experimental Biology; Bethesda, MD.: 1976.

Anderson DJ, Hetzer MW. Nuclear envelope formation by chromatin-mediated reorganization of the endoplasmic reticulum. Nat. Cell Biol. 2007; 9:1160–6. doi:10.1038/ncb1636. [PubMed: 17828249]

Barg S, Galvanovskis J, Gopel SO, Rorsman P, Eliasson L. Tight coupling between electrical activity and exocytosis in mouse glucagon-secreting alpha-cells. Diabetes. 2000; 49:1500–1510. doi: 10.2337/diabetes.49.9.1500. [PubMed: 10969834]

Bencosme, S.; Pease, DC. [6.18.14] Electron Microscopy of the Pancreatic Islets [WWW Document].. Endocrinology. 1958. URL http://press.endocrine.org/doi/pdf/10.1210/endo-63-1-1

Bennett AE, Narayan K, Shi D, Hartnell LM, Gousset K, He H, Lowekamp BC, Yoo TS, Bliss D, Freed EO, Subramaniam S. Ion-abrasion scanning electron microscopy reveals surface-connected tubular conduits in HIV-infected macrophages. PLoS Pathog. 2009; 5 doi:10.1371/journal.ppat. 1000591.

Björkman N, Hellerström C, Hellman B. The ultrastructure of the islets of Langerhans in normal and obese-hyperglycemic mice. Zeitschrift für Zellforsch. und Mikroskopische Anat. 1963; 58:803–819. doi:10.1007/BF00320321.

Bonner-Weir, S. The microvasculature of the pancreas, with emphasis on that of the islets of Langerhans. In: Go, VLW., editor. The Pancreas: Biology, Pathobiology, and Disease. Raven Press; New York: 1993. p. 759-768.

Briggman KL, Helmstaedter M, Denk W. Wiring specificity in the direction-selectivity circuit of the retina. Nature. 2011; 471:183–8. doi:10.1038/nature09818. [PubMed: 21390125]

Brissova M, Fowler MJ, Nicholson WE, Chu A, Hirshberg B, Harlan DM, Powers AC. Assessment of human pancreatic islet architecture and composition by laser scanning confocal microscopy. J. Histochem. Cytochem. 2005; 53:1087–97. doi:10.1369/jhc.5C6684.2005. [PubMed: 15923354]

Cabrera O, Berman DM, Kenyon NS, Ricordi C, Berggren P-O, Caicedo A. The unique cytoarchitecture of human pancreatic islets has implications for islet cell function. Proc. Natl. Acad. Sci. U. S. A. 2006; 103:2334–9. doi:10.1073/pnas.0510790103. [PubMed: 16461897]

Cai T, Hirai H, Zhang G, Zhang M, Takahashi N, Kasai H, Satin LS, Leapman RD, Notkins AL. Deletion of Ia-2 and/or Ia-2β in mice decreases insulin secretion by reducing the number of dense core vesicles. Diabetologia. 2011; 54:2347–2357. doi:10.1007/s00125-011-2221-6. [PubMed: 21732083]

Camussi G, Zanone M, Favaro E. From endothelial to β Cells: Insights into pancreatic islet microendothelium. Curr. Diabetes Rev. 2008; 4:1–9. doi:10.2174/157339908783502415. [PubMed: 18220689]

Carter JD, Dula SB, Corbin KL, Wu R, Nunemaker CS. A practical guide to rodent islet isolation and assessment. Biol. Proced. Online. 2009; 11:3–31. doi:10.1007/s12575-009-9021-0. [PubMed: 19957062]

Cavalier-Smith T. Economy, speed and size matter: Evolutionary forces driving nuclear genome miniaturization and expansion. Annals of Botany. 2005:147–175. doi:10.1093/aob/mci010. [PubMed: 15596464]

Christoffersson G, Henriksnäs J, Johansson L, Rolny C, Ahlström H, Caballero-Corbalan J, Segersvärd R, Permert J, Korsgren O, Carlsson P-O, Phillipson M. Clinical and experimental pancreatic islet transplantation to striated muscle: establishment of a vascular system similar to that in native islets. Diabetes. 2010; 59:2569–78. doi:10.2337/db10-0205. [PubMed: 20651296]

Dai C, Brissova M, Reinert RB, Nyman L, Liu EH, Thompson C, Shostak A, Shiota M, Takahashi T, Powers AC. Pancreatic islet vasculature adapts to insulin resistance through dilation and not angiogenesis. Diabetes. 2013; 62:4144–53. doi:10.2337/db12-1657. [PubMed: 23630302]

Dean PM. Ultrastructural morphometry of the pancreatic β-cell. Diabetologia. 1973; 9:115–119. doi: 10.1007/BF01230690. [PubMed: 4577291]

Denk W, Horstmann H. Serial block-face scanning electron microscopy to reconstruct three-dimensional tissue nanostructure. PLoS Biol. 2004; 2:e329. doi:10.1371/journal.pbio.0020329. [PubMed: 15514700]

Drobne, D. 3D imaging of cells and tissues by focused ion beam/scanning electron microscopy (FIB/SEM). In: Sousa, AA.; Kruhlak, MJ., editors. Nanoimaging SE - 16, Methods in Molecular Biology. Humana Press; 2013. p. 275-292.doi:10.1007/978-1-62703-137-0_16

Fava E, Dehghany J, Ouwendijk J, Müller A, Niederlein A, Verkade P, Meyer-Hermann M, Solimena M. Novel standards in the measurement of rat insulin granules combining electron microscopy, high-content image analysis and in silico modelling. Diabetologia. 2012; 55:1013–23. doi: 10.1007/s00125-011-2438-4. [PubMed: 22252472]

Gregory TR. Genome size evolution in animals. The Evolution of the Genome. 2005:3–87.

Gromada J, Franklin I, Wollheim CB. Alpha-cells of the endocrine pancreas: 35 years of research but the enigma remains. Endocr. Rev. 2007; 28:84–116. doi:10.1210/er.2006-0007. [PubMed: 17261637]

Hekking LHP, Lebbink MN, De Winter DAM, Schneijdenberg CTWM, Brand CM, Humbel BM, Verkleij AJ, Post JA. Focused ion beam-scanning electron microscope: Exploring large volumes of atherosclerotic tissue. J. Microsc. 2009; 235:336–347. doi:10.1111/j.1365-2818.2009.03274.x. [PubMed: 19754727]

Helmstaedter M, Briggman KL, Turaga SC, Jain V, Seung HS, Denk W. Connectomic reconstruction of the inner plexiform layer in the mouse retina. Nature. 2013; 500:168–74. doi:10.1038/nature12346. [PubMed: 23925239]

Holcomb PS, Hoffpauir BK, Hoyson MC, Jackson DR, Deerinck TJ, Marrs GS, Dehoff M, Wu J, Ellisman MH, Spirou G. Synaptic inputs compete during rapid formation of the calyx of Held: a new model system for neural development. J. Neurosci. 2013; 33:12954–69. doi:10.1523/JNEUROSCI.1087-13.2013. [PubMed: 23926251]

Hoppa MB, Jones E, Karanauskaite J, Ramracheya R, Braun M, Collins SC, Zhang Q, Clark a, Eliasson L, Genoud C, Macdonald PE, Monteith a G. Barg S, Galvanovskis J, Rorsman P. Multivesicular exocytosis in rat pancreatic β-cells. Diabetologia. 2012; 55:1001–12. doi:10.1007/s00125-011-2400-5. [PubMed: 22189485]

Huang Y-C, Rupnik MS, Karimian N, Herrera PL, Gilon P, Feng Z-P, Gaisano HY. In situ electrophysiological examination of pancreatic α cells in the streptozotocin-induced diabetes model, revealing the cellular basis of glucagon hypersecretion. Diabetes. 2013; 62:519–30. doi:10.2337/db11-0786. [PubMed: 23043159]

Hughes L, Towers K, Starborg T, Gull K, Vaughan S. A cell-body groove housing the new flagellum tip suggests an adaptation of cellular morphogenesis for parasitism in the bloodstream form of Trypanosoma brucei. J. Cell Sci. 2013; 126:5748–57. doi:10.1242/jcs.139139. [PubMed: 24127564]

Khan FA, Goforth PB, Zhang M, Satin LS. Insulin activates ATP-sensitive K+ channels in pancreatic β-cells through a phosphatidylinositol 3-kinase-dependent pathway. Diabetes. 2001; 50:2192–2198. doi:10.2337/diabetes.50.10.2192. [PubMed: 11574397]

Kharouta M, Miller K, Kim A, Wojcik P, Kilimnik G, Dey A, Steiner DF, Hara M. No mantle formation in rodent islets -- the prototype of islet revisited. Diabetes Res. Clin. Pract. 2009; 85:252–7. doi:10.1016/j.diabres.2009.06.021. [PubMed: 19595468]

Kim A, Miller K, Jo J, Kilimnik G, Wojcik P, Hara M. Islet architecture: A comparative study. Islets. 2009; 1:129–36. doi:10.4161/isl.1.2.9480. [PubMed: 20606719]

Kiseleva E, Morozova KN, Voeltz GK, Allen TD, Goldberg MW. Reticulon 4a/NogoA locates to regions of high membrane curvature and may have a role in nuclear envelope growth. J. Struct. Biol. 2007; 160:224–35. doi:10.1016/j.jsb.2007.08.005. [PubMed: 17889556]

Lacy PE. Electron microscopic identification of different cell types in the islets of langerhans of the guinea pig, rat, rabbit and dog. Anat. Rec. 1957; 128:255–267. doi:10.1002/ar.1091280209. [PubMed: 13458840]

Lacy PE, Davies J. Preliminary studies on the demonstration of insulin in the islets by the fluorescent antibody technique. Diabetes. 1957; 6:354–357. doi:10.2337/diab.6.4.354. [PubMed: 13447765]

Lazarus SS, Volk BW. Studies on a latent diabetic state in cortisone-alloxan treated rabbits. Diabetes. 1964; 13:54–59. doi:10.2337/diab.13.1.54. [PubMed: 14104176]

Like AA, Chick WL. Studies in the diabetic mutant mouse: I. Light microscopy and radioautography of pancreatic islets. Diabetologia. 1970; 6:207–215. doi:10.1007/BF01212231. [PubMed: 4914661]

Liu YM, Guth PH, Kaneko K, Livingston EH, Brunicardi FC. Dynamic in vivo observation of rat islet microcirculation. Pancreas. 1993; 8:15–21. [PubMed: 8419903]

Michael DJ. Pancreatic cells secrete insulin in fast- and slow-release forms. Diabetes. 2006; 55:600–607. doi:10.2337/diabetes.55.03.06.db05-1054. [PubMed: 16505221]

Mikami S, Mutoh K. Light- and electron-microscopic studies of the pancreatic islet cells in the chicken under normal and experimental conditions. Zeitschrift für Zellforsch. und Mikroskopische Anat. 1971; 116:205–227. doi:10.1007/BF00331262.

Munger BL, Caramia F, Lacy PE. The ultrastructural basis for the identification of cell types in the pancreatic islets. Zeitschrift für Zellforsch. und Mikroskopische Anat. 1965; 67:776–798. doi:10.1007/BF00339301.

Murakami T, Fujita T, Miyake T, Ohtsuka A, Taguchi T, Kikuta A. The insuloacinar portal and insulo-venous drainage systems in the pancreas of the mouse, dog, monkey and certain other animals: a scanning electron microscopic study of corrosion casts. Arch. Histol. Cytol. 1993; 56:127–47. [PubMed: 8373657]

Mustafi D, Kevany BM, Genoud C, Bai X, Palczewski K. Photoreceptor phagocytosis is mediated by phosphoinositide signaling. FASEB J. 2013; 27:4585–95. doi:10.1096/fj.13-237537. [PubMed: 23913857]

Neumann FR, Nurse P. Nuclear size control in fission yeast. J. Cell Biol. 2007; 179:593–600. doi:10.1083/jcb.200708054. [PubMed: 17998401]

Noske AB, Costin AJ, Morgan GP, Marsh BJ. Expedited approaches to whole cell electron tomography and organelle mark-up in situ in high-pressure frozen pancreatic islets. J. Struct. Biol. 2008; 161:298–313. doi:10.1016/j.jsb.2007.09.015. [PubMed: 18069000]

Nyman LR, Wells KS, Head WS, McCaughey M, Ford E, Brissova M, Piston DW, Powers AC. Real-time, multidimensional in vivo imaging used to investigate blood flow in mouse pancreatic islets. J. Clin. Invest. 2008; 118:3790–7. doi:10.1172/JCI36209. [PubMed: 18846254]

Ohtani O. Review of scanning electron and light microscopic methods in microcirculation research and their application in pancreatic studies. Scan. Electron Microsc. 653–61. 1984

Olofsson CS, Göpel SO, Barg S, Galvanovskis J, Ma X, Salehi A, Rorsman P, Eliasson L. Fast insulin secretion reflects exocytosis of docked granules in mouse pancreatic β-cells. Pflugers Arch. 2002; 444:43–51. doi:10.1007/s00424-002-0781-5. [PubMed: 11976915]

Orci L. A portrait of the pancreatic β-Cell. Diabetologia. 1974; 10:163–187. doi:10.1007/BF00423031. [PubMed: 4602673]

Orci L. Macro- and micro-domains in the endocrine pancreas. Diabetes. 1982; 31:538–565. doi:10.2337/diab.31.6.538. [PubMed: 6759269]

Pérez-Armendariz M, Roy C, Spray DC, Bennett MV. Biophysical properties of gap junctions between freshly dispersed pairs of mouse pancreatic beta cells. Biophys. J. 1991; 59:76–92. doi:10.1016/S0006-3495(91)82200-7. [PubMed: 2015391]

Pinali C, Bennett H, Davenport JB, Trafford AW, Kitmitto A. Three-dimensional reconstruction of cardiac sarcoplasmic reticulum reveals a continuous network linking transverse-tubules: this organization is perturbed in heart failure. Circ. Res. 2013; 113:1219–30. doi:10.1161/CIRCRESAHA.113.301348. [PubMed: 24044951]

Prado CL, Pugh-Bernard AE, Elghazi L, Sosa-Pineda B, Sussel L. Ghrelin cells replace insulin-producing beta cells in two mouse models of pancreas development. Proc. Natl. Acad. Sci. U. S. A. 2004; 101:2924–9. doi:10.1073/pnas.0308604100. [PubMed: 14970313]

Schneider CA, Rasband WS, Eliceiri KW. NIH Image to ImageJ: 25 years of image analysis. Nat Meth. 2012; 9:671–675.

Schneider P, Meier M, Wepf R, Müller R. Towards quantitative 3D imaging of the osteocyte lacuno-canalicular network. Bone. 2010; 47:848–58. doi:10.1016/j.bone.2010.07.026. [PubMed: 20691297]

Sobota JA, Ferraro F, Bäck N, Eipper BA, Mains RE. Not all secretory granules are created equal: Partitioning of soluble content proteins. Mol. Biol. Cell. 2006; 17:5038–52. doi:10.1091/mbc.E06-07-0626. [PubMed: 17005911]

Stagner JI, Samols E. Retrograde perfusion as a model for testing the relative effects of glucose versus insulin on the A cell. J. Clin. Invest. 1986; 77:1034–7. doi:10.1172/JCI112356. [PubMed: 3512599]

Steiner DJ, Kim A, Miller K, Hara M. Pancreatic islet plasticity: interspecies comparison of islet architecture and composition. Islets. 2010; 2:135–45. [PubMed: 20657742]

Stendahl JC, Kaufman DB, Stupp SI. Extracellular matrix in pancreatic islets: relevance to scaffold design and transplantation. Cell Transplant. 2009; 18:1–12. [PubMed: 19476204]

Straub SG, Shanmugam G, Sharp GWG. Stimulation of insulin release by glucose is associated with an increase in the number of docked granules in the beta-cells of rat pancreatic islets. Diabetes. 2004; 53:3179–3183. doi:10.2337/diabetes.53.12.3179. [PubMed: 15561948]

Unger RH, Orci L. Physiology and pathophysiology of glucagon. Physiol. Rev. 1976; 56:778–826. [PubMed: 185634]

Walton J. Lead asparate, an en bloc contrast stain particularly useful for ultrastructural enzymology. J. Histochem. Cytochem. 1979; 27:1337–1342. doi:10.1177/27.10.512319. [PubMed: 512319]

Webster M, Witkin KL, Cohen-Fix O. Sizing up the nucleus: nuclear shape, size and nuclear-envelope assembly. J. Cell Sci. 2009; 122:1477–86. doi:10.1242/jcs.037333. [PubMed: 19420234]

West JB, Fu Z, Deerinck TJ, Mackey MR, Obayashi JT, Ellisman MH. Structure-function studies of blood and air capillaries in chicken lung using 3D electron microscopy. Respir. Physiol. Neurobiol. 2010; 170:202–209. doi:10.1016/j.resp.2009.12.010. [PubMed: 20038456]

Westermark P, Li Z-C, Westermark GT, Leckström A, Steiner DF. Effects of beta cell granule components on human islet amyloid polypeptide fibril formation. FEBS Lett. 1996; 379:203–206. doi:10.1016/0014-5793(95)01512-4. [PubMed: 8603689]

Winborn WB. Light and electron microscopy of the islets of langerhans of the saimiri monkey pancreas. Anat. Rec. 1963; 147:65–93. doi:10.1002/ar.1091470107. [PubMed: 14062367]

Young RD, Knupp C, Pinali C, Png KMY, Ralphs JR, Bushby AJ, Starborg T, Kadler KE, Quantock AJ. Three-dimensional aspects of matrix assembly by cells in the developing cornea. Proc. Natl. Acad. Sci. U. S. A. 2014; 111:687–92. doi:10.1073/pnas.1313561110. [PubMed: 24385584]

Zhang G, Hirai H, Cai T, Miura J, Yu P, Huang H, Schiller MR, Swaim WD, Leapman RD, Notkins AL. RESP18, a homolog of the luminal domain IA-2, is found in dense core vesicles in pancreatic islet cells and is induced by high glucose. J. Endocrinol. 2007; 195:313–321. doi:10.1677/JOE-07-0252. [PubMed: 17951542]

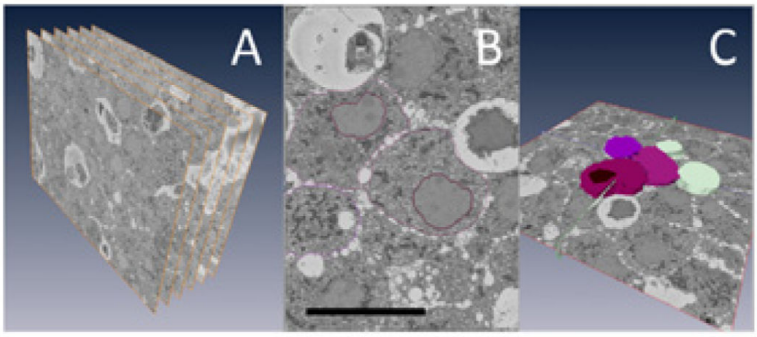

Fig 1.

Serial block-face SEM data of a mouse islet of Langerhans: (A) SBF-SEM can produce a series of hundreds or even thousands of orthoslices, a small sample of which is shown here. (B, C) Following acquisition, orthoslice series are rendered into 3-D ultrastructure by manual segmentation. B represents a single segmented slice, one of many that together build up the rendering shown in C. Bar = 10 μm.

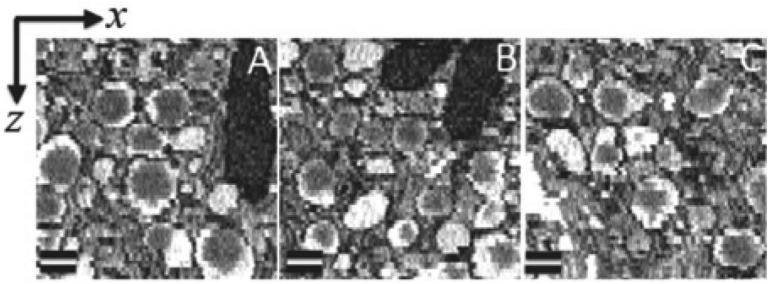

Fig. 2.

Three sub-regions (A-C) containing secretory granules of a pancreatic islet beta cell shown in the *x*-*z* plane; pixel size in x-direction is 5.4 nm, and pixel size in z-direction is 25 nm, as determined by the slice thickness. These images indicate that the dense cores of the insulin-containing secretory granules are round and the well-defined membranes surrounding the granule halos are generally continuous and smooth, which is consistent with uniform cutting by the diamond knife. Bar = 200 nm.

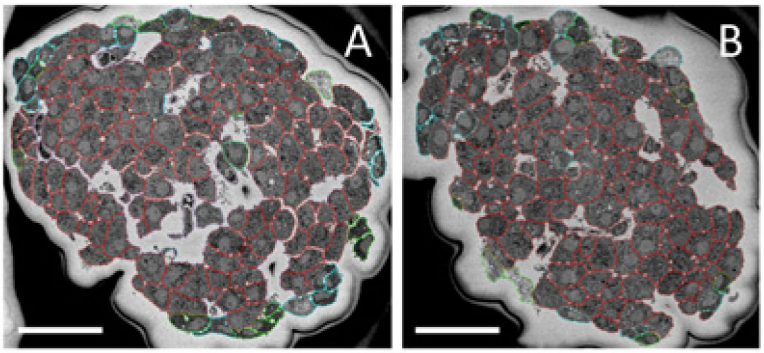

Fig. 3.

Two different islets shown at the global scale: beta cells are outlined in red, alpha cells in blue, and other/unidentified cells in green. Many in the green category are suspected to be somatostatin-secreting delta cells, but it is difficult to make a positive identification. (A) Islet 1, which has a long axis of 233 ± 5 μm and a short axis of 164 ± 5 μm, comprises 77% beta, 14% alpha, and 9% other cell types. (B) Islet 2, with long and short axes of 226 ± 5 μm and 154 ± 5 μm, respectively, consists of 81% beta, 12% alpha, and 7% other cell types. Dark areas surrounding the islets are the result of electrical charging of unstained embedding material. Bar = 50 μm.

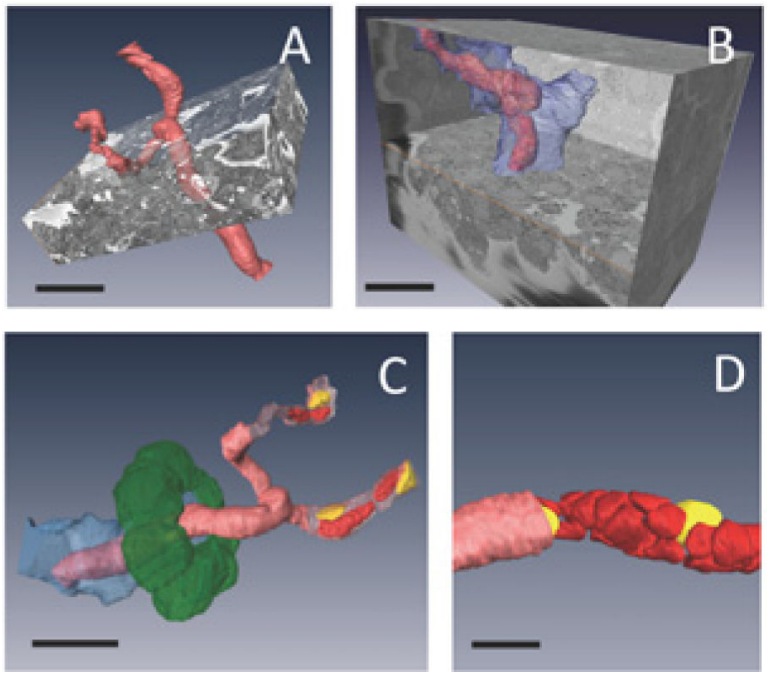

Fig. 4.

Islet's microvasculature: (A, B) two independently branching blood vessels are shown in the context of their surrounding islet cells. A displays the rendered blood vessel (pink red), and B displays the rendered blood vessel and surrounding pericapillary space (blue), illustrating how much volume is occupied by each pericapillary space in an islet. Bar = 20 μm. (C) The different layers of the blood vessel are shown: a representative ring of beta cells surrounding the pericapillary space (green), the pericapillary space (blue), the endothelial-cell lining of the capillary (pink red), and the blood cells (bright red) and endothelial nuclei (yellow) inside the capillary. Bar = 20 μm. (D) The pattern of tight packing of blood cells (bright red) and endothelial nuclei (yellow) is more clearly shown for a different branch of the capillary. Bar = 10 μm.

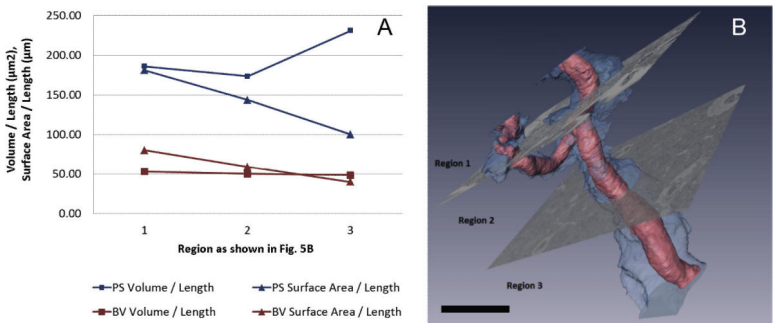

Fig 5.

(A) Volume-to-length and surface area-to-length ratios for the pericapillary space (PS) and blood vessel (BV) in each of the three regions shown in B. Bar = 20 μm.

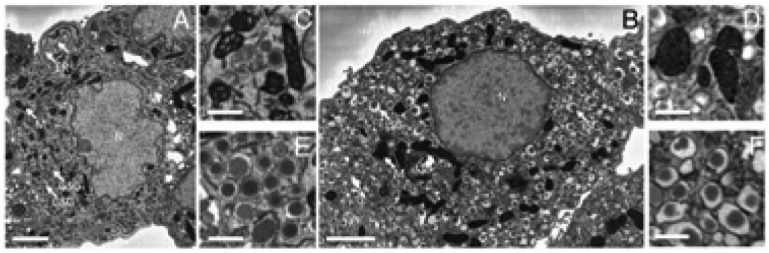

Fig. 6.

Morphological distinctions between alpha and beta cells: serial block-face SEM orthoslices facilitate comparison of alpha and beta cell morphology. Complete cross-sectional views of typical alpha (A) and beta (B) cells evince several characteristic differences between the two cell types, including the greater cytoplasmic lucency of the alpha cell and the rounder nucleus of the beta cell. Bar = 2 μm. In magnified views, alpha cell mitochondria (C) show more visible cristae membranes than exhibited by beta mitochondria (D). Bar = 0.5 μm. Magnified views also highlight that the alpha cell's glucagon-secreting granules (E) have smaller, rounder halos than the beta cell's insulin-secreting ones (F). Bar = 0.5 μm. ER, endoplasmic reticulum; M, mitochondria; N, nucleus; ISGs, insulin-secreting granules; GSGs, glucagon-secreting granules.

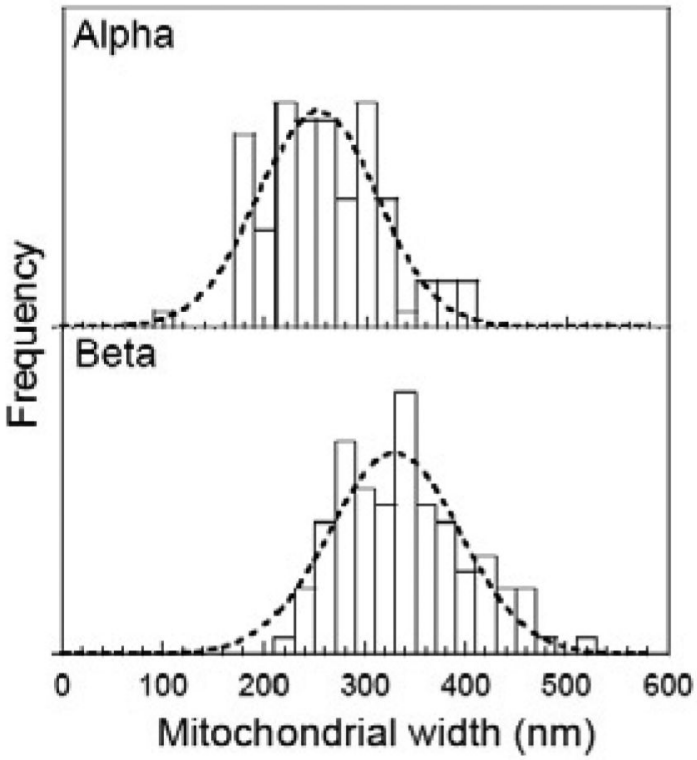

Fig. 7.

Measured widths of mitochondria in alpha and beta cells in 3D SBF-SEM image stacks obtained by finding the largest cross sectional views of each structure. Mitochondria in beta cells are significantly wider (329±92 nm) compared to mitochondria in alpha cells (253±83 nm); dashed lines are fitted Gaussian curves.

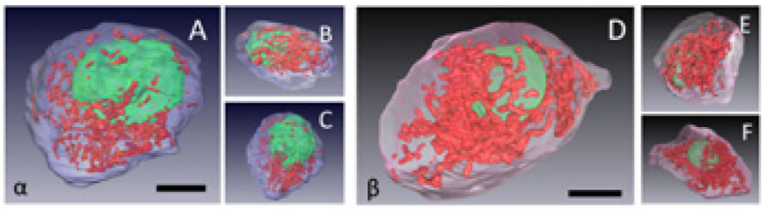

Fig. 8.

Full 3-D surface rendering of a typical alpha and a typical beta cell: (A – C) different views of an alpha cell display the plasma membrane (blue), nucleus (green), and mitochondria (red). This cell had a measured volume of 570 ± 14 μm^3, a nuclear volume of 126 ± 3 μm^3, and a mitochondrial volume of 25 ± 1 μm^3. Bar = 5 μm. (D – F) Different views of a beta cell display the plasma membrane (pink), nucleus (green), and mitochondria (red). This cell had a measured volume of 1,010 ± 30 μm^3, a nuclear volume of 115 ± 3 μm^3, and a mitochondrial volume of 73 ± 5 μm^3. Bar = 5 μm.

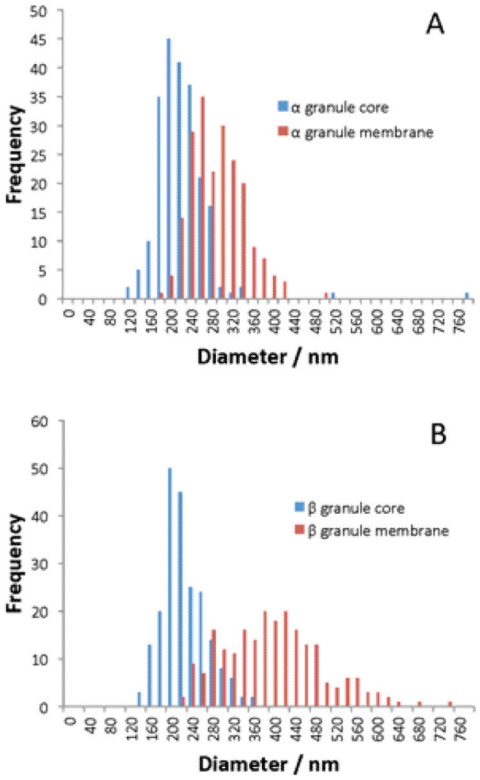

Fig. 9.

Histograms show the size distributions of: (A) glucagon-secreting granules in alpha cells, and (B) insulin-secreting granules in beta cells. For each cell type diameters of dense cores are shown in blue and diameters of secretory granule membranes in red.

Table 1

Calculated physical parameters for one entire, independently branching, blood vessel and its surrounding pericapillary space and cells. Errors in volume and surface area of blood vessel and pericapillary space were based on variations in measurements using 10 successive segmentations of the same structure, which resulted in a standard deviation of 2.5% (lines 1-4). The error in the volume fraction of the pericapillary space was based on the propagation of measurement errors for the pericapillary volume and the islet volume (line 5). For 10 cells that were close to the pericapillary space surrounding the blood vessel, it was difficult to determine from the images whether or not they actually touched, so the uncertainty in the number of cells touching the pericapillary space was estimated as ±5 (line 6). The average cellular contact area with the pericapillary space as a percentage of cell surface area was measured for the 103 contacting cells and the error is expressed as the standard deviation (line 7).

Total volume of blood vessel	3,100 ± 80 μm^3
Total surface area of blood vessel	3,420 ± 90 μm^2
Total volume of pericapillary space	12,300 ± 300 μm^3
Total surface area of pericapillary space	8,200 ± 200 μm^2
Volume fraction of pericapillary space in islet	0.090 ± 0.003
Number of cells touching pericapillary space	103 ± 5
Average cellular contact area with pericapillary space as percentage of cell surface area	9 ± 5 %

Table 2

Size parameters of alpha and beta cells in a typical pancreatic islet, as average values ± standard deviation.

	Average volume / μm^3	N	Average surface area / μm^2	N
Alpha cell				
Total	$5.2 (\pm 1.2) \times 10^2$	30	$5.1 (\pm 1.1) \times 10^2$	10
Nucleus	$1.3 (\pm 0.12) \times 10^2$	20	$2.1 (\pm 0.31) \times 10^2$	10
Mitochondria	$1.9 (\pm 0.43) \times 10^1$	6	$4.0 (\pm 0.93) \times 10^2$	6
Beta cell				
Total	$9.3 (\pm 1.4) \times 10^2$	30	$7.7 (\pm 0.71) \times 10^2$	10
Nucleus	$1.2 (\pm 0.13) \times 10^2$	20	$1.5 (\pm 0.15) \times 10^2$	10
Mitochondria	$7.2 (\pm 1.6) \times 10^1$	6	$1.0 (\pm 0.16) \times 10^3$	6

Table 3

Average diameter (± standard deviation) of the core and membrane of alpha cell GSGs and beta cell ISGs.

	Average diameter / nm	N
Alpha cell		
Granule core	2.3 (± 0.58) × 10^2	215
Granule membrane	3.0 (± 0.51) × 10^2	203
Beta cell		
Granule core	2.4 (± 0.42) × 10^2	212
Granule membrane	4.1 (± 0.97) × 10^2	219